Model-based robust pose estimation for a multi-segment, programmable bevel-tip steerable needle

Alberto Favaro[1], Riccardo Secoli[2], Ferdinando Rodriguez y Baena[2], and Elena De Momi[1]

Abstract—**Bevel-tip steerable needles for percutaneous intervention are prone to torsion determined by the interaction forces with the human tissue. If disregarded, torsion can affect the insertion accuracy inducing a change in the needle tip orientation, which is generally undetectable by tracking devices because of the small diameter of the needle. This paper presents a method for estimating the tip pose (i.e. position and orientation) of a programmable bevel-tip needle using a 2-D kinematic based Extended Kalman Filter (EKF), where the tip position of the two steering segments is used as input measurement. Simulation trials and experiments in phantom-brain gelatin were performed to prove the performance of the method and mimic real case scenarios. The solution presented shows state-of-the-art performance in needle pose estimation with a bounded positional error of $< 1\mathrm{mm}$ and orientation error of $< 5^{\circ}$.**

Index Terms—**Medical Robots and Systems; Surgical Robotics: Steerable Catheters/Needles; Biologically-Inspired Robots**

I. INTRODUCTION

PERCUTANEOUS needle insertion is a common medical approach used for procedures such as biopsy, brachytherapy, drug delivery and thermal ablation to achieve minimally-invasive access to different organs and body regions as the breast, kidney, liver, prostate and brain [1], [2]. In these contexts, this approach is often preferred to standard open surgery for the reduced tissue trauma and the faster recovery time. Nonetheless, percutaneous interventions can be challenging when the targeted tissue is deep inside the body due to the presence of anatomical structures to be avoided and the onset of needle deflection caused by tissue inhomogeneity and deformation [3].

Recent effort has been applied to the design of steerable percutaneous needles, the steering of which can be robotically controlled so as to perform nonstraight paths, allowing the needle to avoid the anatomical obstacles and increase tip placement accuracy [4]. These include the Programmable Bevel-tip Needle (PBN), a multi-segment steerable needle composed of four axially-interlocked slender sections, which are robotically actuated to develop specific tip configurations that allow the needle to steer.

A significant component required to bring these robotically-actuated steerable needles into use is the development of appropriate control strategies to achieve an accurate insertion. This can be obtained in a closed-loop fashion if the position and the orientation of the needle (i.e. its full pose) are known. This is not trivial in flexible needles as the tip is not rigidly connected to the base. Needle tracking methods can thus be used, as X-Ray fluoroscopy [5], ultrasound (US) [6][7] and electromagnetic (EM) tracking systems [8]. However, imaging methods cannot track the rotation of the needle about its insertion axis (the roll angle) because of its small diameter [1], which also precludes the possibility to accommodate a 6 Degrees of Freedom (DoF) EM sensor. Some authors [6], [9], [10], handled this limitation by considering the roll angle at the needle tip as equal to the one measured at the base, assuming an infinite torsional stiffness of the needle.

For the PBN, closed-loop control was achieved by using adaptive control strategies to compensate for unknown, nonlinear mechanical properties [11], [12]. More recently, these non-linearities were modelled by using finite-element techniques [13], creating a new optimised control for the configuration of the segments.

For most of the steerable needle designs, the effect of needle-tissue interactions determines a significant torsional moment. In the case of PBNs, for some tip configurations, experiments demonstrated the onset of an unmodelled needle torsion during the insertion, ascribed to needle-tissue shear forces, which can increase the error in tracking if not measured and subsequently compensated for.

Reed *et al.* [14] proposed a solution to model the torsion experienced by a bevel-tip needle controlled through base rotation. This model was later expanded by Swensen *et al.* [15] with a length-varying torsional dynamics component. They introduced it in a closed-loop control framework in combination with C-arm fluoroscopy imaging for needle position tracking. Kallem *et al.* [16] presented a feedback controller that stabilizes a bevel-tip steerable needle to a desired 2-D plane. In their work, they used the 3-D needle tip position and estimated the needle torsion applying a Luenberger observer to the reduced and feedback-linearized Webster's model of the needle [17]. These works, however, are designed for a steerable needle that strongly differs from the PBN in terms

Manuscript received: December, 23, 2019; Revised: May, 20, 2020; Accepted: June, 14, 2020.

This paper was recommended for publication by Editor P. Valdastri upon evaluation of the Associate Editor and Reviewers' comments. *This project has received founding from the European Unions Horizon 2020 research and innovation program under grant agreement No 688279.

[1]NearLab, Department of Electronics, Information and Bioengineering Department (DEIB), Politecnico di Milano, 20133, Milan, Italy alberto.favaro@polimi.it, elena.demomi@polimi.it

[2]Mechatronics In Medicine Laboratory, Mechanical Engineering Department, Imperial College London, U.K. f.rodriguez@imperial.ac.uk

Digital Object Identifier (DOI): see top of this page.

of structure, kinematics and steering mechanism [11], making them unsuitable for this type of needle.

A solution for the full pose tracking of a PBN was proposed by Khan *et al.* [18], where multi-core optical fibers with embedded Fiber Bragg Grating sensors were used. Errors in pose reconstruction were identified since the fibers are not bonded to the needle and can thus experience a different level of torsion with respect to the needle body.

In this paper, a solution for estimating the full pose of a PBN during the insertion is proposed, which addresses the case of needle torsion. A simplified version of the PBN, featuring two axially-interlocked segments, is considered (sPBN). For some configurations, this PBN design has shown experimentally to be affected by the onset of a torsional effect around the insertion axis. The method involves an Extended Kalman Filter (EKF) defined on the 2-D kinematic model of the sPBN originally presented by Ko et al. in [19] and properly extended to contemplate the torsion of the needle. In order to mock up a real test scenario where conventional imaging systems are used, only the position of the tip of the two needle segments is considered as a measurement to estimate the full 6DoF pose. As target accuracy for needle pose estimation, in the proposed method we considered a position and orientation of $< 1\mathrm{mm}$ and $< 5°$, respectively, in line with [5], [16].

Such a solution can be used as a means to inform the PBN control system about the pose taken by the needle during the insertion process, allowing the controller to compensate for the potential onset of needle torsion.

II. METHODS

A. Needle kinematic model

The sPBN needle can generate controlled steering in a plane according to the relative offset between the two active beveled-tip segments, as shown in the schematic representation of Fig. 1a. The two segments are identified as *A* and *B*. Their local frames, $\mathbf{X}_A$ and $\mathbf{X}_B$, are on the segments tips.

The needle kinematic model described in [19] is:

$$\begin{bmatrix}\dot{x}\\ \dot{y}\\ \dot{\psi}\\ \dot{\delta}\end{bmatrix} = \begin{bmatrix}\cos(\psi)\\ \sin(\psi)\\ k_1(\delta-\epsilon\psi)\\ 0\end{bmatrix} v_1 + \begin{bmatrix}0\\0\\0\\1\end{bmatrix} v_2 \tag{1}$$

where x, y represent the *x*-axis and *y*-axis coordinates of the rear segment frame ($\mathbf{X}_r$) with respect to the global reference frame *O*. Based on the needle configuration, $\mathbf{X}_r$ can either be $\mathbf{X}_A$ or $\mathbf{X}_B$, according to whether segment *A* or segment *B* is in front. In Fig. 1a, $\mathbf{X}_r$ is $\mathbf{X}_B$ while the leading segment ($\mathbf{X}_l$) is $\mathbf{X_A}$. ψ is the angle of rotation of the tip around the *z*-axis and δ is defined as the relative offset between the two segments at the needle base (see Fig. 1a). v_1 is the cruise speed, i.e. the forward velocity of the whole needle body, while v_2 is the offset velocity, i.e the rate of change of δ.

The sPBN is formed by two segments able to slide relatively to each other. According to this principle, when the needle bends, the inner part of $\mathbf{X}_l$ is in compression and the inner part of $\mathbf{X}_r$ is in tension, resulting in a difference between the offset at the tip (δ_t) and offset at the base (δ). As reported in [19], the relationship between the two offsets is:

$$\delta_t = \delta - \epsilon\psi \tag{2}$$

with $\epsilon = (8R_n)/(3\pi)$ for a needle made by two segments, where R_n the radius of the needle.

The rotational velocity $\dot{\psi}$ is linked to the cruise speed v_1 as follows:

$$\dot{\psi} = \rho v_1 \tag{3}$$

where ρ is the instantaneous curvature that the needle tip follows. In Ko et al. [19], ρ is considered as proportional to δ_t with a coefficient k_1 as follows:

$$\rho = k_1\delta_t \tag{4}$$

and, from (2), the expression of $\dot{\psi}$ reported in (1) is obtained.

At each time step, δ_t defines the leading segment and the rear segment, such as:

$$\delta_t > 0 \begin{cases}\mathbf{X}_l = \mathbf{X}_A\\ \mathbf{X}_r = \mathbf{X}_B\end{cases} \quad \delta_t < 0 \begin{cases}\mathbf{X}_l = \mathbf{X}_B\\ \mathbf{X}_r = \mathbf{X}_A\end{cases} \tag{5}$$

When the offset of the tip is null, i.e. $\delta_t = 0$, frames $\mathbf{X}_l$ and $\mathbf{X}_r$ coincide. Their poses with respect to the world frame *O* are ${}^O\mathbf{T}_l = {}^O\,\mathbf{T}_r$.

When $\delta_t \neq 0$, a steering angle ξ is shown between $\mathbf{X}_l$ and $\mathbf{X}_r$ [19] (see Fig. 1a), expressed as:

$$\xi = k_1\ \delta_t^2\ \mathrm{sgn}(\delta_t) \tag{6}$$

The radius of curvature (R_c) associated with the angle ξ is defined as:

$$R_c = \frac{\delta_t}{\xi}\mathrm{sgn}(\delta_t) \tag{7}$$

The translation ${}^r\mathbf{P}_l$ from $\mathbf{X}_r$ to $\mathbf{X}_l$ (in Fig. 1a, respectively $\mathbf{X}_B$ and $\mathbf{X}_A$) is defined as:

$${}^r\mathbf{P}_l = [R_c\ \sin(\xi), R_c(1-\cos(\xi)), 0]^T \tag{8}$$

The transformation ${}^r\mathbf{T}_l$ between $\mathbf{X}_r$ and $\mathbf{X}_l$ is defined as:

$${}^r\mathbf{T}_l = \begin{bmatrix} & \mathbf{R}_z(\xi) & & {}^r\mathbf{P}_l\\ 0 & 0 & 0 & 1\end{bmatrix} \tag{9}$$

where $\mathbf{R}_z(\xi)$ is the rotation between $\mathbf{X}_r$ and $\mathbf{X}_l$ due to the presence of ξ. The transformation ${}^O\mathbf{T}_l$ between *O* and $\mathbf{X}_l$ can be computed as:

$${}^O\mathbf{T}_l = {}^O\,\mathbf{T}_r\,{}^r\mathbf{T}_l \tag{10}$$

B. Needle torsion

Differences in the roll angle (ϕ) between the tip and the base are a well-known fact for needles that require rotation to steer [16], [20]. In the case of the sPBN, the needle undergoes a torsion because of the interaction between the needle tip and the tissue when an offset δ_t is generated, or for frictional components between segments. This torsion determines a rotation by an angle ϕ about the x-axis that drives the needle from an ideal 2-D motion to a 3-D displacement (see Fig. 1b) and an orientation discrepancy between the needle tip and the base, which does not rotate.

This is the author's version of an article that has been published in this journal. Changes were made to this version by the publisher prior to publication.
The final version of record is available at http://dx.doi.org/10.1109/LRA.2020.3018406

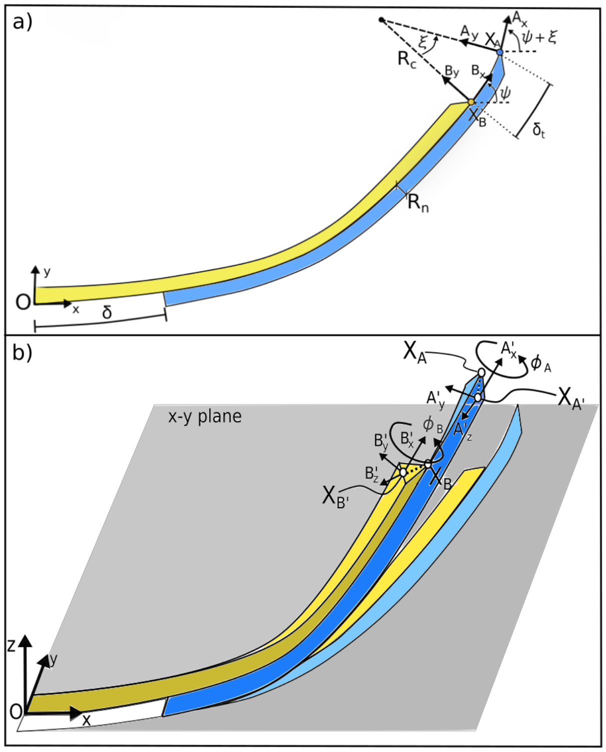

Fig. 1: *Needle kinematics:* in a), a 2-D representation of the two-segment sPBN is reported. $\mathbf{X}_A$ and $\mathbf{X}_B$ represent the local frames of segment A and segment B. In the case depicted, $\mathbf{X}_A = \mathbf{X}_l$ and $\mathbf{X}_B = \mathbf{X}_r$. R_n is the needle radius and δ the offset at the needle base. ψ is the rotation of the needle about the z-axis. The offset at the tip, δ_t, differs from δ because of the needle bend, which generates a further curvature ξ associated to a radius R_c. In b), the effect of needle torsion on the original 2-D trajectory of segment A and B is reported. The needle moves from a planar steering to a spatial movement. The local frames of segment A and segment B are reported. The offset between the leading segment (here the segment A) and the rear segment (here the segment B) determines a different torsion on their tips, i.e $\phi_A \neq \phi_B$.

The poses of the two segments tip become:

$$ {}^{O}\mathbf{T}'_r = \mathbf{R}_x(\phi_r)\,{}^{O}\mathbf{T}_r \tag{11} $$

and

$$ {}^{O}\mathbf{T}'_l = \mathbf{R}_x(\phi_l)\,{}^{O}\mathbf{T}_r\,{}^{r}\mathbf{T}_l \tag{12} $$

where ϕ_l and ϕ_r are the torsion angles on $\mathbf{X}_l$ and $\mathbf{X}_r$, as depicted in Fig. 1b.

C. Needle pose estimation

The state vector $\mathbf{x}$ describes the needle status and is defined as follows:

$$ \mathbf{x} = [x, y, \psi, \delta, k_1, \phi_A, \dot{\phi}_A, \ddot{\phi}_A, \phi_B, \dot{\phi}_B, \ddot{\phi}_B]^T \tag{13} $$

where the first 5 parameters come from (1). The torsion experienced by the two segments enters in the state vector by ϕ_A and ϕ_B. Torsion is assumed to have a second order dynamics: the torsion affecting the sPBN changes during the insertion as a function of the current offset δ_t and can increase or reduce its speed according to the acceleration determined by variations in δ_t during the insertion. Higher order derivatives are modelled by the process noise.

The extended kinematic model, is defined as:

$$ \mathbf{x}(k+1) = f(\mathbf{x}(k)) + b(\mathbf{u}(k+1)) + n(k+1) \tag{14} $$

where $\mathbf{u}$ is the vector of inputs made of the cruise speed and the offset velocity:

$$ \mathbf{u} = [v_1, v_2]^T \tag{15} $$

The process noise $n(k)$ is assumed to be drawn from a zero-mean normal distribution $n(k) \sim \mathcal{N}(0, \mathbf{Q}_p)$ with variance $\mathbf{Q}_p$.

The function $f(\cdot)$ is defined as:

$$ f(\mathbf{x}(k)) = \begin{bmatrix} \mathrm{I}_{[5\times5]} & & 0 \\ & \mathrm{A}_{[3\times3]} & \\ 0 & & \mathrm{A}_{[3\times3]} \end{bmatrix} \begin{bmatrix} x(k) \\ y(k) \\ \psi(k) \\ \delta(k) \\ k_1(k) \\ \phi_A(k) \\ \dot{\phi}_A(k) \\ \ddot{\phi}_A(k) \\ \phi_B(k) \\ \dot{\phi}_B(k) \\ \ddot{\phi}_B(k) \end{bmatrix} \tag{16} $$

where I is the identity matrix and $\mathbf{A}$ describes a second-order dynamics:

$$ \mathbf{A} = \begin{bmatrix} 1 & \Delta t & \frac{1}{2}\Delta t^2 \\ 0 & 1 & \Delta t \\ 0 & 0 & 1 \end{bmatrix} \tag{17} $$

where Δt is the sampling time.

The control-input function $b(\cdot)$ is defined as:

$$ b(\mathbf{u}(k+1)) = \begin{bmatrix} \cos(\psi(k))\Delta t & 0 \\ \sin(\psi(k))\Delta t & 0 \\ k_1(\delta(k) - \epsilon\psi(k))\Delta t & 0 \\ 0 & \Delta t \\ \vdots & \vdots \\ 0 & 0 \end{bmatrix}_{[11\times2]} \begin{bmatrix} v_1(k+1) \\ v_2(k+1) \end{bmatrix} \tag{18} $$

The proposed method makes use of the 3DoF position of the two segments tips. Such information can be obtained through embedded sensors, e.g. EM sensors, or via a suitable imaging modality, such as ultrasound. In case of sensors mounted on the segments tip, a further translation is included to link the sensor local frame to the segments tip, as in Fig. 1b. The sensor local frames, $\mathbf{X}_{A'}$ and $\mathbf{X}_{B'}$, result from the transformation ${}^{O}\mathbf{T}_{A'}$ and ${}^{O}\mathbf{T}_{B'}$, including translations $\Delta S^{A}_{x,y,z}$, $\Delta S^{B}_{x,y,z}$ from the segments tip to the sensors position. For the sake of simplicity, no rotation is assumed in ${}^{O}\mathbf{T}_{A'}$ and ${}^{O}\mathbf{T}_{B'}$.

The observation at time k is expressed as:

$$ y(k) = h(\mathbf{x}(k)) + v(k) \tag{19} $$

where the measurement function $h(\cdot)$ is a non-linear function defined as:

$$ h(\mathbf{x}(t)) = [\mathbf{p}_A, \mathbf{p}_B]^T \tag{20} $$

where $\mathbf{p}$ are the translation component of ${}^{O}\mathbf{T}_{A'}$ and ${}^{O}\mathbf{T}_{B'}$. The measurement noise $v(k)$ is a zero-mean Gaussian noise $v(k) \sim$

$\mathcal{N}(0, \mathbf{Q}_m)$. Variance $\mathbf{Q}_m$ is unknown a-priori and has to be guess in the filter calibration on the basis of the experimental data.

At each time step, the pose of the segments tip $\mathbf{X}_A$ and $\mathbf{X}_B$ can be computed from the parameters in the state vector $\mathbf{x}$ through (11) and (12).

III. Experimental Protocol

A. Simulation study

The EKF was tested over a set of simulated insertions. These tests aimed at evaluating the accuracy of our pose estimation method with respect to the noise within the measurement data so as to determine the maximum level of noise that still guarantees acceptable estimation performance.

A set composed by four variable offset velocities (v_2), reported in Fig. 2a, was provided to the 2-D kinematic model described in Section II-A to generate four simulated needle insertions.

Two 3DoF position sensors were ideally mounted on the segments tips, located at a known distance ($\Delta S^A_{x,y,z}, \Delta S^B_{x,y,z}$) with respect to the tip reference frames ($\mathbf{X}_A$, $\mathbf{X}_B$). The insertions feature different values of k_1, used to obtain different steering responses. These dimensions and parameters are reported in Tab. I.

To mimic the torsion of the needle during the insertion, a rotation ϕ about the needle insertion axis was simulated for both the needle segments at every time step.

We simulated ϕ within the leading segment by applying the following function:

$$\phi_l(t) = \begin{cases} \phi_l(t-1) + \Delta\phi(\delta_t(t)) \\ \qquad\qquad \text{if } |\phi_l(t-1)| < \phi_{max} \\ \\ \phi_l(t-1) + \Delta\phi(\delta_t(t)) e^{-d|\phi_l(t-1) - \phi_{max}|} \\ \qquad\qquad \text{if } |\phi_l(t-1)| \geq \phi_{max} \end{cases} \tag{21}$$

where $\Delta\phi$ represents the incremental step of rotation affecting the leading segment. ϕ_{max} is the maximum angle of needle torsion after which we assumed that the needle torsional compliance would decrease. This limits further rotations, which was simulated by the exponential decay that multiplies $\Delta\phi$ in the second case of (21).

$\Delta\phi$ is defined as follows:

$$\Delta\phi(\delta_t) = \mathrm{sgn}(\delta_t) \cdot \left[\frac{a}{1 + e^{(-b(\delta_t - c))}} - \frac{a}{1 + e^{bc}} \right] \tag{22}$$

we assumed $\Delta\phi$ having a quasi-linear behavior. Values of δ_t near to zero induce a slow increase in the rotation angle; the slope of $\Delta\phi$ rises for larger values of δ_t up to $|\delta_t| \geq 15$mm, where the incremental step of rotation becomes constant. The second addendum in (22) is required to have $\Delta\phi(0) = 0°$. $\Delta\phi$ is symmetrical about the y axis, thus positive values of δ_t drive the needle to twist toward positive values of ϕ and vice-versa. Such a behaviour, designed for the scope of simulation and reported in Fig.2b, represents an assumption based on experimental evidence [13]. Parameters of (21) and (22), reported in Tab. I, were defined empirically on the basis of the expected needle behavior and the experimental evidence.

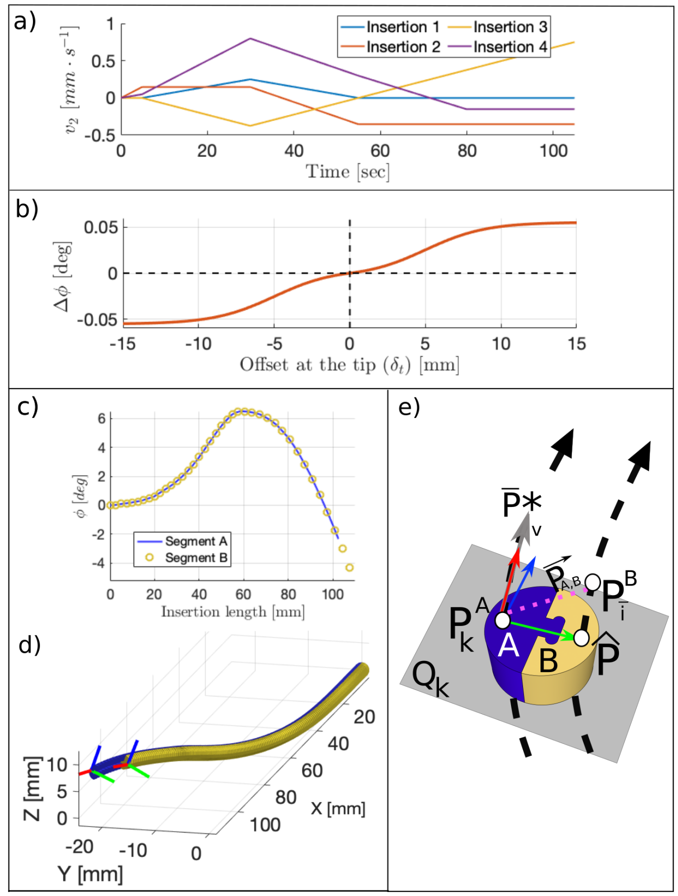

Fig. 2: In a) the evolution of the offset velocities (v_2) for the four simulated insertions is shown over time. In b), the incremental step of needle rotation is reported with respect to the offset at the tip. In c), the trend of ϕ for one simulated insertion is depicted over the insertion length for segment A and B. In d), the resulting 3-D reconstruction of the needle shape. In e), a schematic of the main entities coming into play in the geometric approach is reported.

We hypothesised a follow-the-leader condition for which, at a specific insertion length *l*, the rear segment features an angle of torsion ϕ_r equal to the one shown earlier by the leading segment at the same insertion length, i.e. $\phi_r(l) = \phi_l(l)$.

Fig.2c reports the torsion angle featured by segments A and B in one of the simulated insertions. The resulting needle shape is illustrated by the 3-D reconstructions in Fig. 2d.

White noise with different levels of standard deviation (σ) was used in different simulations. As the lower value of noise, $\sigma_1 = 0.07$mm measured in-gelatin during a static EM acquisition was considered (EM sensors: 5DoF, 0.3mm diameter, Aurora^{TM}, NDI®, Waterloo, Ontario, Canada). As performance metrics for needle position estimation, the Euclidean error (E_t) between the true segment position and the estimated one was used. The orientation error (E_r) was computed individually for each Euler angle as the absolute error between the true angle and the estimated one. We considered as acceptance criteria $E_t < 1$mm and $E_r < 5°$, comparable with the state of the art [5], [16]. With these criteria, an upper bound σ_4 was defined, which is reported in

This is the author's version of an article that has been published in this journal. Changes were made to this version by the publisher prior to publication.
The final version of record is available at http://dx.doi.org/10.1109/LRA.2020.3018406

Needle							**EKF**		**Noise** (σ [mm])			
R_n [mm]	ΔS^A [mm]			ΔS^B [mm]			Q_p	Q_m [mm]	σ_1	σ_2	σ_3	σ_4
1	-1	-1	0	-1	1	0	10^{-9}	1	0.07	0.14	0.21	0.28

$\mathbf{k}_1[\text{mm}^{-2}]$				**Torsion function**					**Setup**		
$k_{1,1}$	$k_{1,2}$	$k_{1,3}$	$k_{1,4}$	a [deg]	b	c	d	ϕ_{max}[deg]	v_1 [mm/s]	L_i [mm]	f [Hz]
$1.85 \cdot 10^{-4}$	$2 \cdot k_{1,1}$	$5 \cdot k_{1,1}$	$k_{1,1}$	0.06	0.5	5	0.2	60	1	110	10

TABLE I: Parameters and dimensions used in the simulation trials.

Tab. I along with two intermediate steps σ_2 and σ_3 included in the test to evaluate the performance of the solution at different levels of measurement noise. The EKF was tested three times over each insertion and each level of σ. In simulations, Q_m was chosen empirically by tuning the nominal accuracy of the EM sensors used in in-gelatin experiments to the value that guarantees the best estimation performance. Similarly, Q_p was chosen as $Q_p = 10^{-j}$ in the set $j \in [0, ..., 10]$ as the value that provides the best prediction accuracy. Q_m, Q_p, insertion speed (v_1), insertion length (L_i), sample rate (f) and further simulation parameters are reported in Tab. I.

Tests were performed using MATLAB® R2019a, on a MacBook Pro (MacOS 10.14.6, 2,7 GHz Intel Core i5, 8 GB of RAM).

B. Geometric approach for pose estimation

A geometric approach was used as a term of comparison for the proposed EKF solution. This method, run offline, relies only on geometric relationships to compute the pose of segments A and B and consists of the definition of a cross-plane Q_k at each time step, as shown in Fig. 2e. In the following, the description of the method for defining the pose of segment A at time k and point P_k^A is reported.

At first, the insertion direction, v, is defined by finding the point $\bar{P}$ as the average of the n = 25 future insertion points with respect to k:

$$\bar{P} = \frac{1}{n}\sum_{1}^{n}(P_{k+i}^A) \tag{23}$$

$$\mathbf{v} = \frac{\bar{P} - P_k^A}{|\bar{P} - P_k^A|} \tag{24}$$

For a sampling frequency of 2Hz and a cruise speed $v_1 = 1\text{mm}\cdot\text{sec}^{-1}$, n=25 corresponds to 12.5secs of acquisition and 12.5mm of needle insertion.
The plane Q_k is defined as follows:

$$a(x - P_{k,x}^A) + b(y - P_{k,y}^A) + c(z - P_{k,z}^A) = 0 \tag{25}$$

where $a = \mathbf{v}_x;\ b = \mathbf{v}_y;\ c = \mathbf{v}_z$.
From the EM data of segment B, the closest point $P_{\bar{i}}^B$ to Q_k is found, where $\bar{i}$ is such that:

$$\bar{i} = \text{argmin}(\overrightarrow{P^{A,B}} \cdot P_k^A)\ \ \forall i \in [0, k_{end}] \tag{26}$$

where k_{end} is the last sample of the EM acquisition and

$$\overrightarrow{P^{A,B}} = P_i^B - P_k^A \tag{27}$$

The projection $\hat{P}$ of $P_{\bar{i}}^B$ on Q_k is computed and the reference frame at P_k^A is obtained as:

$$\mathbf{x} = \frac{\mathbf{v}}{|\mathbf{v}|};\quad \mathbf{y} = \frac{\hat{P} - P_k^A}{|\hat{P} - P_k^A|};\quad \mathbf{z} = \mathbf{x} \times \mathbf{y} \tag{28}$$

The performance of the geometric method was evaluated in simulation over the different levels of noise. As this set includes the noise measured in gelatin during static EM acquisitions (σ_1), the test aims to demonstrate the suitability of the method to be used as a way to compare phantom-brain gelatin experiments.

Similarly to the EKF, the geometric approach was tested three times for each simulated insertion and noise level.

C. In-gelatin experiments

Three needle insertions were performed on phantom-brain gelatin (10% by weight bovine gelatin - Chef William Powdered Gelatin) to assess the performance of the proposed solution in conditions which replicate real insertion scenarios.

In-gelatin trials were performed using a four-segment PBN design, the details of which can be found in [13]. The PBN is formed by four segments featuring one lumen of 0.3mm each, and an overall outer diameter of 2.5mm for all segments together. To reproduce the sPBN model, the four segments were coupled two by two. We can thus define two couples of segments, cpl_A and cpl_B, with the first controlling the left steering and the second controlling the right steering. In such a way, we transform defacto the four-segment PBN design into a two-segment design with cpl_A and cpl_B representing segment A and segment B.

The EKF requires the tip position of segment A and B as measurement data. This is obtained by accommodating an EM Aurora™ sensor (5DoF, 0.3mm diameter, Northern Digital inc.) inside a lumen of cpl_A and a lumen of cpl_B. Only the 3DoF position of each segment was used as measurement input in the proposed method. This approach was chosen to make the solution feasible also for applications where the orientation cannot be measured. The orientation measurements (pitch and yaw angles) are considered as ground truth to validate the EKF estimation accuracy. As for simulation trials, Q_p and Q_m were set through a tuning process to values that provided the best prediction results, namely $Q_p = 1 \cdot 10^{-3}$ and $Q_m = 1\text{mm}^2$.

The experimental setup is reported in Fig. 3 and described hereinafter. The insertion of the needle was driven by a robotic system composed of four linear actuators (one per each PBN segment). The needle was inserted for 20mm in the gelatin phantom, with all four segments aligned, then the desired offset was generated by pushing a couple of adjacent segments ahead (e.g. cpl_A if $\delta > 0$). The needle was then inserted at a constant cruise speed of $1\text{mm} \cdot \text{sec}^{-1}$, as in previous studies [13], [19], resembling the speed of manual insertion of a standard deep brain stimulation electrode performed by an expert neurosurgeon. Encoders recorded the insertion length of the segments, from which the cruise speed v_1 and the offset velocity v_2 could be computed. A sample rate of 2Hz was used, which was assumed to be appropriate, considering the low magnitude of v_1. A desktop PC with Linux Ubuntu 16.04 operating system running the Robotic Operating System (ROS) was used to control the needle insertion and for data storage.

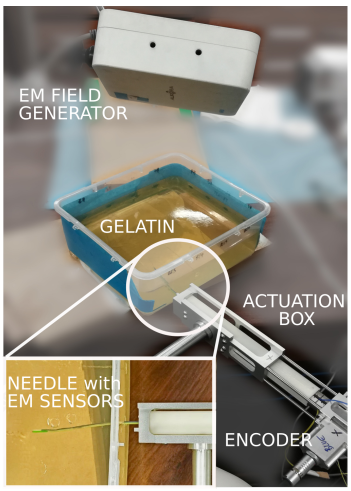

Fig. 3: *Experimental setup:* the PBN is inserted into gelatin and tracked by the EM field generator through the EM sensors mounted on the needle. An actuation box controls each segment of the PBN and encoders measure their insertion length. On the bottom left, a magnification of the needle insertion.

IV. Results

A. Simulation study

The results of simulated trajectories at the different levels of measurement noise are reported in Fig. 4 for the EKF and the geometric approach. As no significant difference was detected from segment A and B and from different simulated insertion profiles, results were combined. In the top row, the Euclidean error (E_t) with respect to the reference trajectory is presented for both the estimation methods. E_t shows a positive linear trend over the increasing of σ still maintaining the position error lower than the 1mm margin of acceptability.

The orientation errors (E_r) are reported in the rows below. As a yardstick, the error of $5°$ considered to be acceptable is reported in the graphs, except for θ and ψ in the EKF results, where it was omitted to improve readability, as E_r was found to be particularly small.

For the EKF, the ϕ angle shows the largest error. The $5°$ yardstick is reached for a measurement noise (σ_4) equal to four times the one evidenced in static in-gelatin EM acquisitions (σ_1). This value can be considered the upper bound accuracy for a tracking system to be used with the presented solution.

The geometrical approach guarantees $E_t < 1\text{mm}$ and $E_r < 5°$ for the level of noise σ_1, which is the one evidenced in-gelatin during static EM measurements, confirming the feasibility of the method to be used as comparison for the experiments in gelatin.

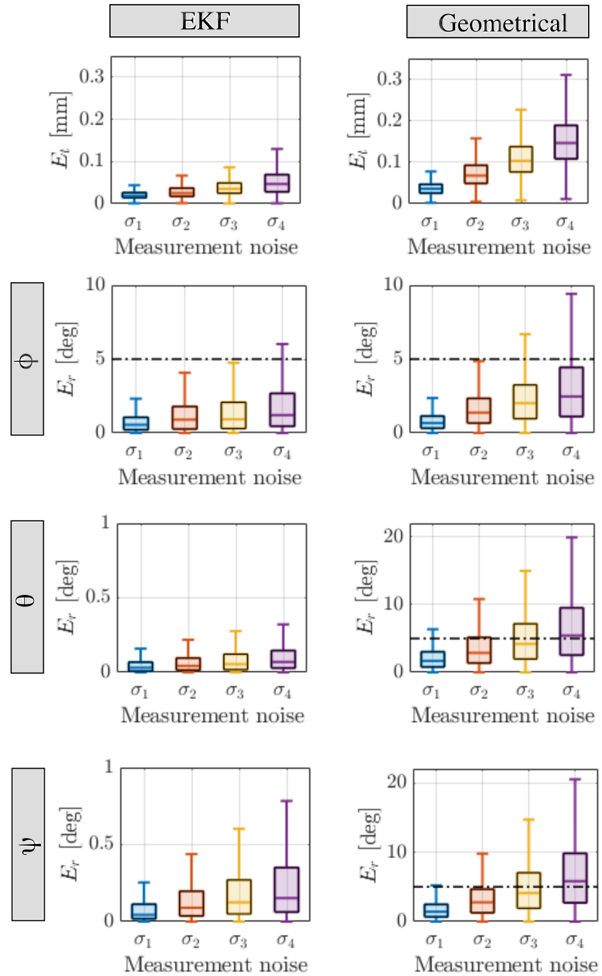

Fig. 4: *Simulation results:* the graphs show Euclidean and orientation errors (E_t, E_r) from the simulation trials at different values of noise (σ). Results from the EKF and the geometrical approach are shown in the left and right columns. As a yardstick, the $5°$ error tolerance is plotted, with the exception of the θ and ψ angles of the EKF where E_r is too small. Please note that the span of the *y* differs for the two methods in the θ and ψ angles.

B. In-gelatin experiments

In Tab. II, the results in terms of E_t and E_r from the 3 in-gelatin insertions are reported as the 25^{th}, 50^{th}, 75^{th} quantiles. Results from the EKF estimation are compared to the measurements provided by the EM sensors, i.e. the 3DoF position and 2DoF orientation (pitch and yaw angles). For the roll angle, the error is measured in comparison to the one computed by the geometric approach.

The results from one of the three sPBN insertions in gelatin are reported in Fig. 5 (Trial 1 in Tab. II). On the left, the original position data retrieved by the two EM sensors embedded in the PBN are reported. On the side, the needle reconstructed from the 6DoF pose estimated by the EKF is shown. In the graphs, the position and the orientation estimated by the EKF are compared to the EM data and the geometric

	E_t [mm]			$E_{r,\phi}$ [deg]			$E_{r,\theta}$ [deg]			$E_{r,\psi}$ [deg]		
	25^{th}	50^{th}	75^{th}	25^{th}	50^{th}	75^{th}	25^{th}	50^{th}	75^{th}	25^{th}	50^{th}	75^{th}
Trial 1	0.10	0.18	0.34	0.62	1.40	2.65	1.97	2.55	3.06	0.82	1.37	1.80
Trial 2	0.11	0.23	0.39	1.98	2.77	4.74	0.69	1.41	2.21	0.79	1.52	2.22
Trial 3	0.32	0.40	0.47	2.71	3.71	4.91	0.27	0.43	0.76	0.53	1.11	1.44

TABLE II: Results from the in-gelatin trials. Position error E_t is computed with respect to the original EM data. Orientation error $E_{r,\phi}$ is computed with respect to the geometric approach, while $E_{r,\theta}$ and $E_{r,\psi}$ relative to the EM data. For each index of performance, the 25^{th}, 50^{th}, 75^{th} quantiles are reported.

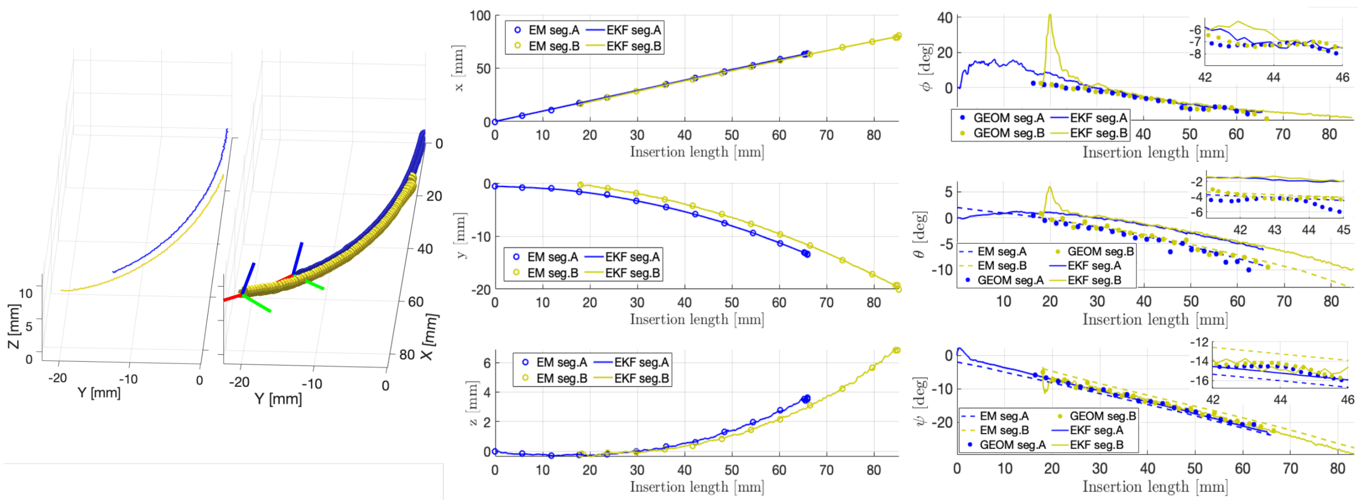

Fig. 5: *In-gelatin results:* on the left, the original position data from the EM sensors are reported for Trial 1. On the side, the reconstruction of the needle from the 6DoF pose estimation by the EKF is reported. Graphs on the left side allow the comparison between the original EM position and the one estimated by the EKF. Graphs on the right side allow to compare the estimated orientation with respect to the EM data (θ and ψ) and the geometric approach (ϕ). A close look at the estimated angles is possible through the three magnification windows reported on the right graphs.

approach (for the roll angle, only the comparison with the geometric approach is possible). For the sake of readability, in the graphs, the EM position data and the needle orientation reconstructed using the geometric approach are under-sampled by a factor 25 and 10, respectively.

EKF results show an initial phase of orientation convergence, particularly evident for the roll angle. This phase is measured as the insertion length required to stabilize the needle within the 5° error margin with respect to the angles provided by the geometric approach, neglecting the initial insertion offset between segments. In Fig. 5, the convergence phase for Trial 1, segment B, was found to be equal to 8mm. The convergence phases measured for Trial 2 and Trial 3 are 7.5mm and 10mm in duration, respectively. The convergence phase is overlooked in the computation of the position and orientation errors of Tab. II.

V. Discussions

Simulation trials on the EKF demonstrate for the roll angle a less accurate estimation than for the other orientation angles. In the EKF, the roll and its derivatives are unreachable states. For these states, the initial prediction based on model inputs is not possible and, for their estimation, the EKF relies solely on the noisy measurement data, which leads to a higher estimation error. In gelatin, where modeling inaccuracies come into play, the error in pitch and yaw angles becomes similar to the one in the roll.

Compared to the EKF, a faster worsening in pose reconstruction accuracy was evidenced in simulation for the geometric approach over the raise of the measurement noise. Indeed, by filtering the measurement data with the state prediction provided by the needle kinematic model, the EKF can increase the robustness of the estimation in the presence of measurement noise. In addition, the main drawback of the geometric approach consists of the impossibility to compute the needle pose in the parts of the insertion where the needle cross-plane cannot be defined, i.e. in the offset between segments. In the in-gelatin trial reported in Fig. 5, this is represented by the final part of the insertion of segment B, which is the leading segment that defines the steering direction and the pose of which is essential for the sake of needle control. This drawback prevents the geometric approach from being used as a means for pose estimation in real insertion scenarios.

The soundness of the proposed solution is confirmed by the EKF performance in gelatin. Compared to the shape reconstruction solution proposed by Khan *et al.* for a PBN [18], our model-based pose estimation method achieves a reduction in the mean position error of ∼30%. No data are provided in [18] for a comparison of the orientation errors. In this regard, if compared with a steerable needle tracking solution as the model-based approach developed in [6] for a bevel-tip needle, our solution demonstrates similar orientation errors, although in [6] the estimation of the roll angle was overlooked.

To make the proposed solution suitable for applications where only the needle position can be tracked (e.g. where tracking is performed via X-ray fluoroscopy or US), only the 3DoF position of the needle segments tip is considered as tracking data from the 5DoF EM sensors (the pitch and yaw angles are used only as ground truth for validation). Benefits in terms of estimation performance arising from the inclusion of pitch and yaw angles from the 5DoF EM sensors as measurement data will be the object of forthcoming investigations.

Future studies will focus also on improvements derived from the use of different filtering approaches, as the Unscented KF and particle filters, and on adapting the proposed method to the case of the four-segment PBN, the design of which can be viewed as the combination of 2 sPBN orthogonally arranged to achieve movements in 3-D as the sum of a vertical and an horizontal steering. In this regard, the PBN kinematic model proposed in [21] could be extended including the effect of torsion to each needle segment, as in Section II-B. The EKF could be designed around this adapted PBN model in a way similar to Section II-C and the position of the four PBN segments tips be used as measurement data by the filter to estimate the PBN pose during the insertion. Additionally, an adaptation to other types of steerable needles will also be evaluated. A possible candidate is the bevel-tip needle with base rotation, the kinematic model of which is reported in [16]. The needle tip position could be tracked and, similarly to the method herein presented, a state variable representing the torsional mismatch between the tip and the base of the needle could be included in the EKF to correct the needle pose estimation.

VI. Conclusion

In percutaneous intervention, the ability to track the needle position and orientation (i.e. the full pose) is of paramount importance for a robotic steering system to perform accurate needle insertion and address needle torsion. The method herein presented, based on an EKF, uses the position measurement of the needle tip to correct the needle state prediction obtained from a kinematic model and to infer the roll angle. The method is proposed for a two-segment beveled tip needle (sPBN) accommodating a sensor for position tracking within the tip of each segment. The method was tested in simulation, demonstrating reliability in terms of estimation accuracy and robustness against measurement noise. In experiments conducted in gelatin, the solution was able to estimate the needle pose with a position error < 1mm and an orientation error $< 5°$, consistent with the state of the art. The pose estimated by the filter could thus be safely used by a control system to drive the needle insertion and address potential needle torsion.

References

[1] N. J. Cowan, K. Goldberg, G. S. Chirikjian, G. Fichtinger, R. Alterovitz, K. B. Reed, V. Kallem, W. Park, S. Misra, and A. M. Okamura, "Robotic needle steering: Design, modeling, planning, and image guidance," in *Surgical Robotics: Systems Applications and Visions*. Boston, MA: Springer US, 2011, pp. 557–582.

[2] N. Abolhassani, R. Patel, and M. Moallem, "Needle insertion into soft tissue: A survey," *Medical Engineering and Physics*, vol. 29, no. 4, pp. 413–431, 2007.

[3] S. Misra, K. B. Reed, B. W. Schafer, K. T. Ramesh, and A. M. Okamura, "Mechanics of flexible needles robotically steered through soft tissue," *International Journal of Robotics Research*, vol. 29, no. 13, pp. 1640–1660, 11 2010.

[4] N. J. van de Berg, D. J. van Gerwen, J. Dankelman, and J. J. van den Dobbelsteen, "Design Choices in Needle SteeringA Review," *IEEE/ASME Transactions on Mechatronics*, vol. 20, no. 5, pp. 2172–2183, 10 2015.

[5] K. Ralovich, M. John, E. Camus, N. Navab, and T. Heimann, "6DoF catheter detection, application to intracardiac echocardiography," *Medical image computing and computer-assisted intervention : MICCAI ... International Conference on Medical Image Computing and Computer-Assisted Intervention*, vol. 17, no. Pt 2, pp. 635–642, 2014.

[6] G. J. Vrooijink, M. Abayazid, and S. Misra, "Real-time three-dimensional flexible needle tracking using two-dimensional ultrasound," in *Proceedings - IEEE International Conference on Robotics and Automation*. IEEE, 5 2013, pp. 1688–1693.

[7] P. Chatelain, A. Krupa, and M. Marchal, "Real-time needle detection and tracking using a visually servoed 3D ultrasound probe," in *2013 IEEE International Conference on Robotics and Automation*. IEEE, 5 2013, pp. 1676–1681.

[8] H. Sadjadi, K. Hashtrudi-Zaad, and G. Fichtinger, "Needle deflection estimation using fusion of electromagnetic trackers," in *2012 Annual International Conference of the IEEE Engineering in Medicine and Biology Society*. IEEE, 8 2012, pp. 952–955.

[9] N. Shahriari, E. Hekman, M. Oudkerk, and S. Misra, "Design and evaluation of a computed tomography (CT)-compatible needle insertion device using an electromagnetic tracking system and CT images," *International Journal of Computer Assisted Radiology and Surgery*, vol. 10, no. 11, pp. 1845–1852, 11 2015.

[10] M. Abayazid, P. Moreira, N. Shahriari, S. Patil, R. Alterovitz, and S. Misra, "Ultrasound-guided three-dimensional needle steering in biological tissue with curved surfaces," *Medical Engineering and Physics*, vol. 37, no. 1, pp. 145–150, 1 2015.

[11] R. Secoli and F. R. Y. Baena, "Adaptive path-following control for bio-inspired steerable needles," in *Proceedings of the IEEE RAS and EMBS International Conference on Biomedical Robotics and Biomechatronics*, vol. 2016-July. IEEE, 6 2016, pp. 87–93.

[12] R. Secoli, F. Rodriguez, and Baena, "Experimental validation of curvature tracking with a programmable bevel-tip steerable needle," in *2018 International Symposium on Medical Robotics, ISMR 2018*, vol. 2018-Janua. IEEE, 2018, pp. 1–6.

[13] T. Watts, R. Secoli, and F. R. Y. Baena, "A Mechanics-Based Model for 3-D Steering of Programmable Bevel-Tip Needles," *IEEE Transactions on Robotics*, vol. 35, no. 2, pp. 371–386, 4 2019.

[14] K. Reed, A. Okamura, and N. Cowan, "Modeling and Control of Needles With Torsional Friction," *IEEE Transactions on Biomedical Engineering*, vol. 56, no. 12, pp. 2905–2916, 12 2009.

[15] J. P. Swensen, M. Lin, A. M. Okamura, and N. J. Cowan, "Torsional dynamics of steerable needles: Modeling and fluoroscopic guidance," *IEEE Transactions on Biomedical Engineering*, vol. 61, no. 11, pp. 2707–2717, 11 2014.

[16] V. Kallem and N. J. Cowan, "Image guidance of flexible tip-steerable needles," *IEEE Transactions on Robotics*, vol. 25, no. 1, pp. 191–196, 2 2009.

[17] R. J. Webster, N. J. Cowan, G. Chirikjian, and A. M. Okamura, "Nonholonomic modeling of needle steering," in *Springer Tracts in Advanced Robotics*, 2006, vol. 21, pp. 35–44.

[18] F. Khan, A. Denasi, D. Barrera, J. Madrigal, S. Sales, and S. Misra, "Multi-Core Optical Fibers With Bragg Gratings as Shape Sensor for Flexible Medical Instruments," *IEEE Sensors Journal*, vol. 19, no. 14, pp. 5878–5884, 7 2019.

[19] S. Y. Ko, L. Frasson, and F. Rodriguez Y Baena, "Closed-loop planar motion control of a steerable probe with a programmable bevel inspired by nature," *IEEE Transactions on Robotics*, vol. 27, no. 5, pp. 970–983, 10 2011.

[20] K. B. Reed, A. Majewicz, V. Kallem, R. Alterovitz, K. Goldberg, N. J. Cowan, and A. M. Okamura, "Robot-assisted needle steering," *IEEE Robotics and Automation Magazine*, vol. 18, no. 4, pp. 35–46, 12 2011.

[21] R. Secoli and F. Rodriguez Y Baena, "Closed-loop 3D motion modeling and control of a steerable needle for soft tissue surgery," in *Proceedings - IEEE International Conference on Robotics and Automation*. IEEE, 2013, pp. 5831–5836.